nature communications

Article

https://doi.org/10.1038/s41467-025-60288-1

Deterministic control of nanomagnetic spiral trajectories using an electric field

Received: 12 March 2025

Accepted: 20 May 2025

Published online: 06 June 2025

Check for updates

Samuel H. Moody[1,2,3] ✉, Matthew T. Littlehales[2,4], Daniel A. Mayoh[5], Geetha Balakrishnan[5], Diego Alba Venero[4], Peter D. Hatton[2] & Jonathan S. White[1] ✉

The intertwined nature of magnetic and electric degrees of freedom in magnetoelectric (ME) materials is well described by ME-coupling theory. When an external electric field is applied to a ME material, the ME coupling induces unique and intriguing magnetic responses. Such responses underpin the utilisation of ME materials across diverse applications, ranging from electromagnetic sensing to low-energy digital memory technologies. Here, we use small angle neutron scattering and discover a novel magnetic response within an archetypal chiral ME material, Cu_2OSeO_3. We find that the propagation direction of an incommensurate magnetic spiral is deterministically actuated and deflected along controllable trajectories. Furthermore, we predict the emergence of distinct non-linear regimes of spiral-deflection behaviour with external electric and magnetic fields, unlocking innovative devices that leverage controlled and customisable variations in macroscopic polarisation and magnetisation.

In our increasingly data-driven and environmentally conscious world, the imperative to reduce the impact of electronics while enhancing their functionality is undeniable. Magnetoelectrics (ME) represent a promising avenue in this pursuit, offering highly functional yet sustainable applications. This feature has fostered intense research, both fundamental and for applications ranging from sensing to low-power digital technologies; however, the full richness of the magnetoelectric response of large-scale magnetic structures, such as incommensurate magnetic spirals, remains relatively unexplored.

ME materials are characterised by intertwined electric and magnetic order parameters[1–11]. A ME coupling between these degrees of freedom manifests from various mechanisms, leading to the realisation of a multitude of physical phenomena under the application of an applied electric (E) field[12–19]. Examples include the appearance of concomitant ferromagnetism and ferroelectricity[20–22], the selection of magnetic spiral chirality and domain wall motion[23–26], and control of the stability and orientation of topological magnetic skyrmion lattices[27–29]. These ME coupling effects continually inspire the development of next-generation technological devices, such as low-energy digital memory schemes, advanced sensors,[30], and applications in biology and medicine[31]. Exploring novel magnetoelectric responses to applied E-fields presents an exceptional opportunity to deepen our understanding and engineer devices with tangible real-world impacts.

Large-scale magnetic structures are composed of complex arrangements of many individual spins with periodicities spanning numerous atomic unit cells. This composite nature gives rise to rich emergent behaviour, contrasting significantly with isolated magnetic moments[32–35]. For instance, even in insulators where the magnetic moments are localised at crystallographic sites, large-scale magnetic structures can collectively shrink and expand, coherently reorient, and be driven through a crystalline system[36–38]. Therefore, new physical effects can be anticipated by amalgamating the richness of magnetoelectric responses with novel phenomena associated with the many degrees of freedom in large-scale magnetic structures.

Here, we investigate the E-field driven response of large-scale incommensurate magnetic spiral structures in the archetypal

[1]Laboratory for Neutron Scattering and Imaging (LNS), PSI Center for Neutron & Muon Science, Paul Scherrer Institut (PSI), Villigen, Switzerland. [2]Department of Physics, Durham University, Durham DH1 3LE, United Kingdom. [3]Department for Hydrogen Technology, Institute for Energy Technology, Kjeller, Norway. [4]ISIS Neutron and Muon Source, Rutherford Appleton Laboratory, Didcot, United Kingdom. [5]Department of Physics, University of Warwick, Coventry CV4 7AL, United Kingdom. ✉e-mail: samuel.moody@psi.ch; jonathan.white@psi.ch

magnetoelectric material Cu_2OSeO_3. Using small-angle neutron scattering (SANS) to directly probe these spiral structures, we demonstrate that an applied *E*-field liberates the directional anchoring imposed on the spiral structures by magnetic anisotropies, providing fine control over the propagation direction of the spirals along specific trajectories. Theoretical modelling suggests this propagation-deflection is deterministic and induces measurable variations in both the macroscopic magnetisation and electric polarisation. Moreover, our modelling predicts the existence of distinct regimes of *E*-field-driven spiral-deflection behaviour whose onsets are further tunable by an applied magnetic field, permitting a variety of dynamic *E*-field-driven effects that are ripe for exploitation.

Results and discussion

Figure 1 summarises the magnetic and magnetoelectric properties of Cu_2OSeO_3 for magnetic fields applied along a crystallographic ⟨100⟩ axis. At the atomic level, the unit cell contains sixteen $S = 1/2$ Cu^{2+} ions distributed across two symmetry-distinct Wyckoff sites, which couple to form ferrimagnetic tetrahedra with effective $S = 1$ (See Fig. 1a)[39,40]. These ferrimagnetic building blocks form the magnetic basis that constitutes the large-scale incommensurate magnetic structures. Below $T_C \approx 58$ K, helical windings with a wavelength of the order 60 nm (≈70 times the lattice constant) form the magnetic ground state due to the quantum-driven, multi-length scale nature of the material, stabilising incommensurate magnetism through a complex network of effective interactions between the tetrahedra. The delicate balance of competing effective interactions causes different magnetic structures to lie close together in magnetic free energy[41–43], generating a wealth of many magnetic states that exist at different temperatures and applied magnetic fields, as depicted by the magnetic phase diagram shown in Fig. 1b. At low temperatures (<30 K), unusual magnetic states such as low-temperature skyrmion and tilted conical (TC) states arise due to the increasing significance of higher-order anisotropic interactions[44–47].

The low-temperature magnetic states visualised in Fig. 1c–e are characterised by magnetisation propagating incommensurately along distinct directions. The conical state exhibits a spin-structure with a periodicity along the applied magnetic field, with a component of the magnetisation exhibiting a ubiquitous canting (by a conical angle θ) towards the same direction. This periodicity along a high-symmetry direction causes the electric polarisation to vanish when integrated over a magnetic unit cell. The TC state adopts a similar structure but differs by a characteristic tilting in propagation direction (by angle ϕ) away from the magnetic field. This tilting forces the periodicity of the magnetisation along a low-symmetry direction, generating a finite bulk electric polarisation parallel to the magnetic field direction (See SI). Conversely, zero electric polarisation is realised for low-temperature magnetic skyrmions (topologically protected whirls of magnetisation

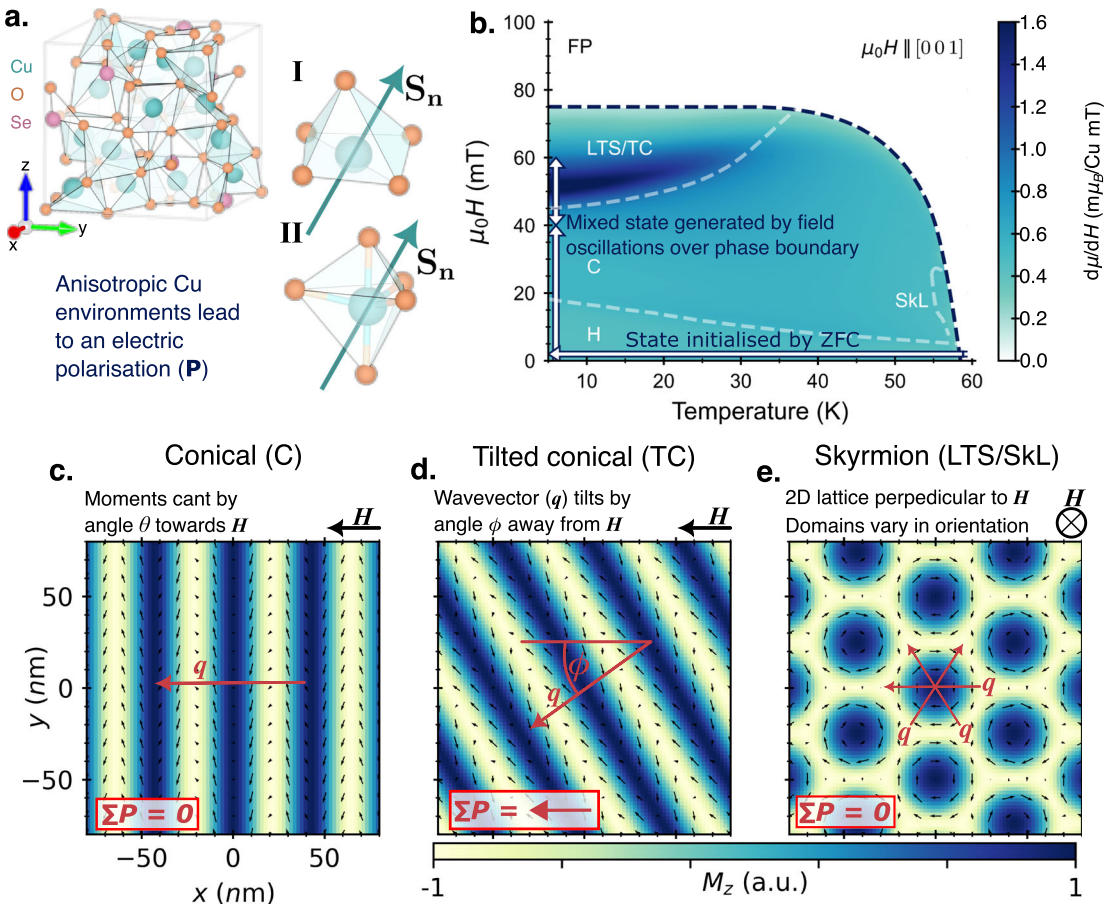

Fig. 1 | Magnetic and electric polarisation properties of Cu_2OSeO_3 for fields along the [001] direction. a Chiral cubic crystal structure of Cu_2OSeO_3 (non-centrosymmetric with space group $P2_13$, point group 23) featuring two symmetry inequivalent copper sites. The relative orientation of the local moment ($\mathbf{S_n}$) within these Cu-sites generates local polarisation via the *d*–*p* hybridisation mechanism, contributing to a net macroscopic polarisation that depends on the propagation direction and the overall nature of the magnetic structure[17,52,53]. **b** Magnetic phase diagram for an applied magnetic field along the crystallographic [001] direction., showing five distinguishable ordered magnetic phases: the helical (H) ground state, conical (C), tilted conical (TC), low-temperature skyrmion (LTS), field polarised (FP), and skyrmion lattice (SkL). **c**–**e** Real-space schematics of the incommensurate spin textures investigated in this study, illustrating variations in the propagation direction (**q**), net electric polarisation ($\Sigma\mathbf{P}$), and their relative orientation to the applied magnetic field ($\mu_0 H$).

https://doi.org/10.1038/s41467-025-60288-1

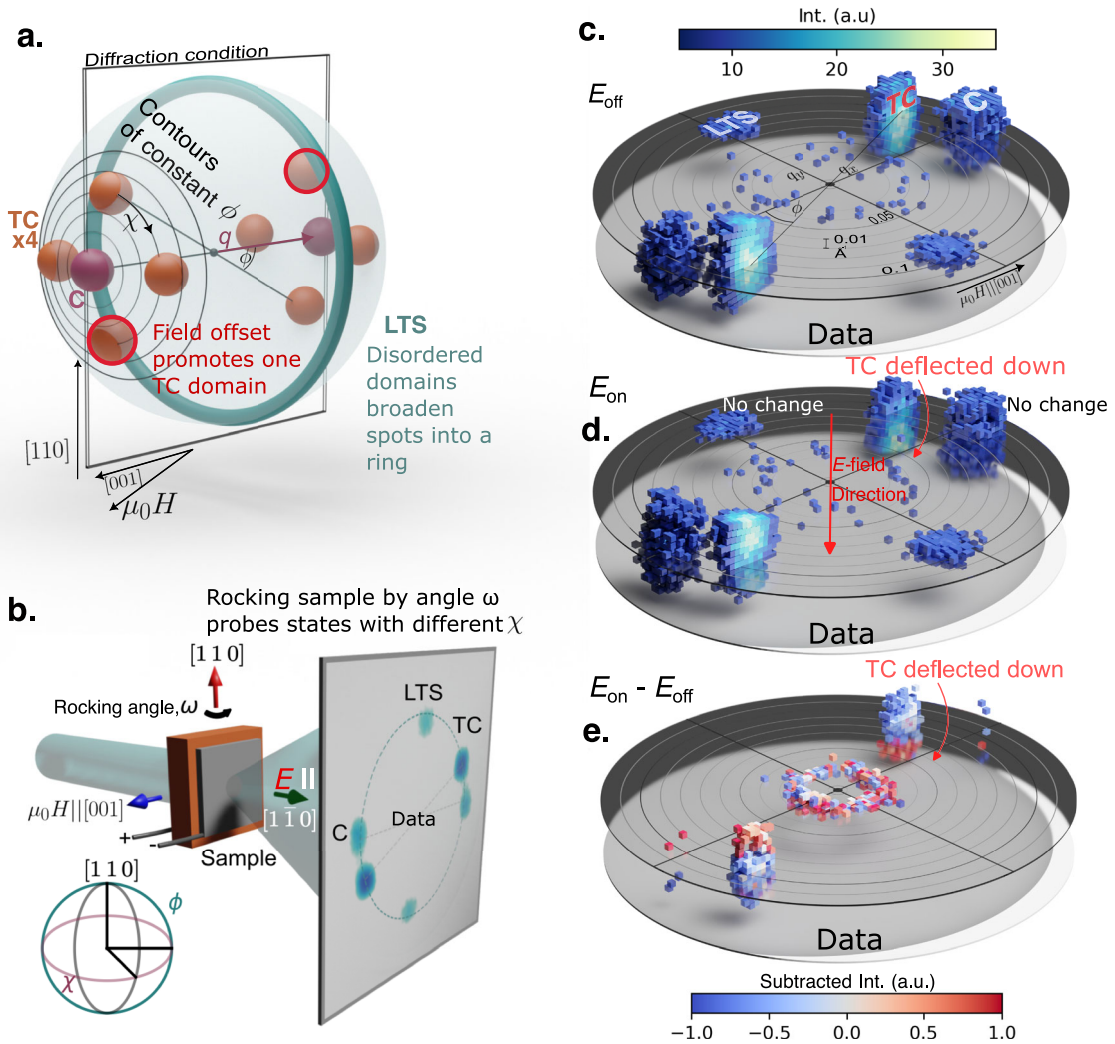

Fig. 2 | Reciprocal space depiction, experimental geometry and three-dimensional tomographic SANS maps. a Schematic of the expected neutron intensity distributions in reciprocal space arising from different incommensurate magnetic phases in Cu_2OSeO_3. The diagram illustrates the applied magnetic field, crystallographic directions, and the diffraction condition for a particular detector plane. **b** Experimental SANS configuration showing the directions of the magnetic and *E*-field relative to the sample and the incoming neutron beam. The detector captures a single exposure, probing the volume of reciprocal space corresponding to the slice depicted above. Rotating about the vertical (ω) axis sweeps the diffraction condition through a volume of reciprocal space, premising our tomographic SANS measurements (See Methods). **c**, **d** Electric field-dependent 3D tomographic SANS maps at $E = 0$ (**c**) and 2500 V/m (**d**) at 5 K. Each voxel contains normalised intensity scattered from a $0.01 \times 0.01 \times 0.01$ 0.01 $Å^{-3}$ volume in reciprocal space, with additional reciprocal space information labelled. The TC spot is cut vertically to highlight the effect of the *E*-field. The deflection trajectory of the TC wavevector is clearly visible in the difference map shown in (**e**).

forming periodic lattices in a plane perpendicular to the applied magnetic field[38,41]) due to the net cancellation of electric charge quadrupoles generated within the core of each magnetic skyrmion for this magnetic field configuration[17].

The periodic nature of the various low-temperature magnetic structures corresponds to particular locations in reciprocal space, linked via the Fourier transform of the real-space magnetisation. These locations are defined by the magnetic wavevector (**q**) of the states and are related to the real-space periodicity (λ) of the structure by $|\mathbf{q}| = \frac{2\pi}{\lambda}$. Due to the different directions of propagation displayed by the spiral textures shown in Fig. 1c–e, their associated magnetic wavevectors align with different directions in Fourier space, as visualised in Fig. 2a. For instance, the magnetic wavevector of the conical state (purple arrow) lies along the field direction, in accordance with the periodicity direction. The characteristic tilting away from the applied field (in the polar-direction–ϕ) of the TC state is evident, and the cubic anisotropy leads to the stabilisation of four symmetry-equivalent TC domains, with propagation directions directed towards different azimuthal angles (χ), corresponding to the four ⟨111⟩ directions. The low-temperature skyrmion state forms with periodicities confined to the plane perpendicular to $\mu_0 H$, and in domains with mutual orientational disorder[46]. Therefore, the associated magnetic wavevectors form a ring in reciprocal space (blue ring in Fig. 2a).

Experimentally, the separation of these magnetic wavevectors in momentum space allows for efficient simultaneous probing of the three magnetic states. SANS is the optimal technique for investigating such large-scale magnetic structures, excelling in obtaining detailed information about the magnetic ordering, periodicity, and orientation of each phase[48]. The experimental geometry is schematically shown in Fig. 2b, summarising the mutual orientations of the crystalline axes, electric and magnetic fields (See Methods for further information). In this setup, magnetic wavevectors differing in ϕ and lying within the detector plane can be observed easily in a single neutron exposure. To collect orientational information along the out-of-plane (χ) direction it is necessary to rock the sample about the vertical axis by an angle, ω.

Our main finding is highlighted by the three-dimensional tomographic reciprocal space maps shown in Fig. 2c–e. We intentionally

https://doi.org/10.1038/s41467-025-60288-1

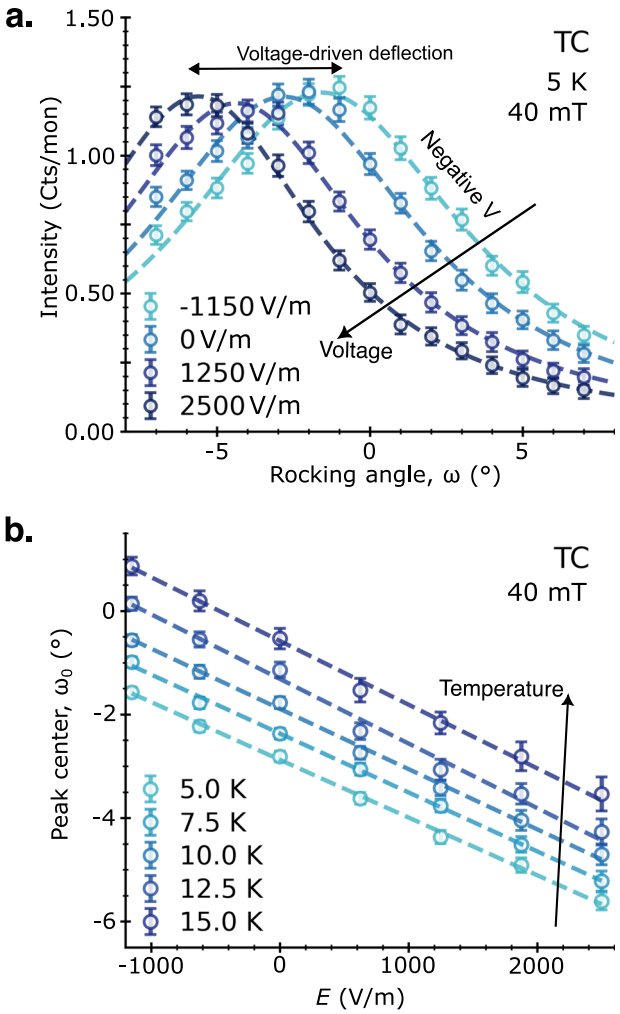

Fig. 3 | Characterisation of the magnetic wavevector trajectory as a function of electric field and temperature. a Diffracted neutron intensity from the TC state as a function of rocking angle, ω, for different applied voltages at 5 K. Horizontal shifts in peak position indicate a change in wavevector corresponding to a deflection of the spiral along the neutron beam direction. **b** *E*-field dependence of this deflection as a function of temperature, with each temperature offset along the *y* axis for clarity. Linear trends are observed in all datasets. Errors correspond to the diagonalised covariance matrix obtained in the fitting procedure.

generated a triple-state coexistence of the conical, TC and low-temperature skyrmion states (See Methods) for both the zero *E*-field ($V = 0$) and finite *E*-field ($V = 2500$ V/m) datasets. For the conical and low-temperature skyrmion states, no *E*-field-induced changes in the observed intensity, peak shape and wavevector are detected, as expected for magnetic textures that do not generate any electric net polarisation. In contrast, we observe a clear *E*-field actuated deflection of the TC magnetic wavevector. The deflection trajectory is out of the diffraction plane along the χ direction, towards the applied *E*-field, and orthogonal to the TC tilt-angle ϕ. This observation marks the first demonstration of such a magnetoelectric deflection response.

Quantitative information on the deflection of the TC texture is presented in Fig. 3a. The integrated neutron intensity from the TC state is presented as a function of the experimental rocking angle, ω. The displacement of the peak center maps the trajectory of the magnetic propagation deflection, which lies along the χ-direction. These trajectories shift towards lower or higher angles, respectively, in response to the magnitude and sign of the applied *E*-field. Fitting these rocking curves to a Gaussian function and extracting the peak center reveals a linear relationship between the deflection angle and the applied *E*-field. This behavior is consistent across a range of temperatures (Fig. 3b), indicating the occurrence of this effect in all regimes where the TC is energetically stable. These experimental results provide an unambiguous and microscopic demonstration of the magnetoelectric deflection of the TC spin-texture, and moreover reveal that the trajectories vary smoothly with the applied *E*-field over the explored parameter space.

To explain our observations, we develop a theoretical framework that describes the physical mechanisms of the TC state stability and the trajectory of the *E*-field actuated magnetoelectric deflection response. Given that the periodicity of the TC state is much greater than the crystallographic unit cell, we employ mean-field theory. Experimentally, we clarify that a TC state nucleates from the conical state upon increasing the magnetic field, as presented in Fig. 4a. By inserting a conical Ansatz into a model Hamiltonian consisting of the standard exchange, Dzyaloshinskii-Moriya and Zeeman interactions[49], we stabilise the TC state by incorporating competing fourth-order magnetocrystalline and exchange anisotropies, using experimentally determined values[45,50,51] (See Methods for more information). Figure 4b shows the expected TC polar angle (ϕ) as function of both the magnetic field and its angle-offset with respect to [001]. By overlaying the experimentally determined values, we find that the model successfully captures the TC nucleation, the magnitude of ϕ-tilting, and eventual collapse with increasing magnetic field. In accordance with the experimental geometry and observations, we reproduce the observed second-order transition into a TC state by including a small field tilt-angle relative to [001] in the model calculations.

Having reproduced the stability of the TC state, we turn our attention to the magnetoelectric coupling. Accounting for the symmetry of the *d*–*p* hybridisation mechanism of magnetoelectric coupling appropriate for chiral cubic systems, the continuous form of the electric polarisation is given by refs. 52,53:

$$\mathbf{P} = (P_x, P_y, P_z) = \lambda_C (m_y m_z, m_x m_z, m_x m_y), \tag{1}$$

where $\{x, y, z\}$ define a basis following the $\langle 100 \rangle$ crystal directions, and λ_C is the bulk saturation polarisation. The TC spin-texture generates a net electric polarisation along the direction of the TC magnetic wavevector projected in the $\phi = 0$ plane, specifically along the magnetic field direction for $\chi = 0$. We explain the observed deflection of the TC state by minimising the magnetoelectric free energy density, $\bar{F}_{MFA} = -\bar{\mathbf{P}} \cdot \mathbf{E}$, which aligns a component of the net electric polarisation along the *E*-field. However, this deflection increases the anisotropy energy, which varies approximately parabolically about the $\chi = 0$ direction for small χ. By expanding the free energy density, integrating over a TC period and differentiating with respect to χ, we find that, in the limit of small *E*, the deflection trajectory is linear and lies along the χ direction:

$$\frac{\partial \chi}{\partial E} \approx \frac{\lambda_C \cos\phi f(\theta)}{\gamma q^2 \sin^2\theta \sin^3\phi + K \sin^4\phi g(\theta)}, \tag{2}$$

where γ, K are, respectively, the anisotropic exchange and magnetocystalline anisotropy constants. The functions, $g(\theta)$ and $f(\theta)$, are trigonometric functions dependent solely on the TC cone angle (See Methods). The linear relationship between the deflection and the applied *E*-field aligns with the experimentally determined trajectory, indicating that the magnetoelectric energy term acts as a perturbation significantly weaker than the anisotropic magnetic interactions. This allows the stability of the TC state to be maintained throughout the entire deflection trajectory. By calculating the expected TC deflection for different values of λ_C, we numerically find that the saturation polarisation required to reproduce the experimental observations is $\lambda_C = 10.4(4) \times 10^{-6}$ C/m^2, in strong agreement with previous macroscopic measurements[17,54]. The physical origin of the deflection

https://doi.org/10.1038/s41467-025-60288-1

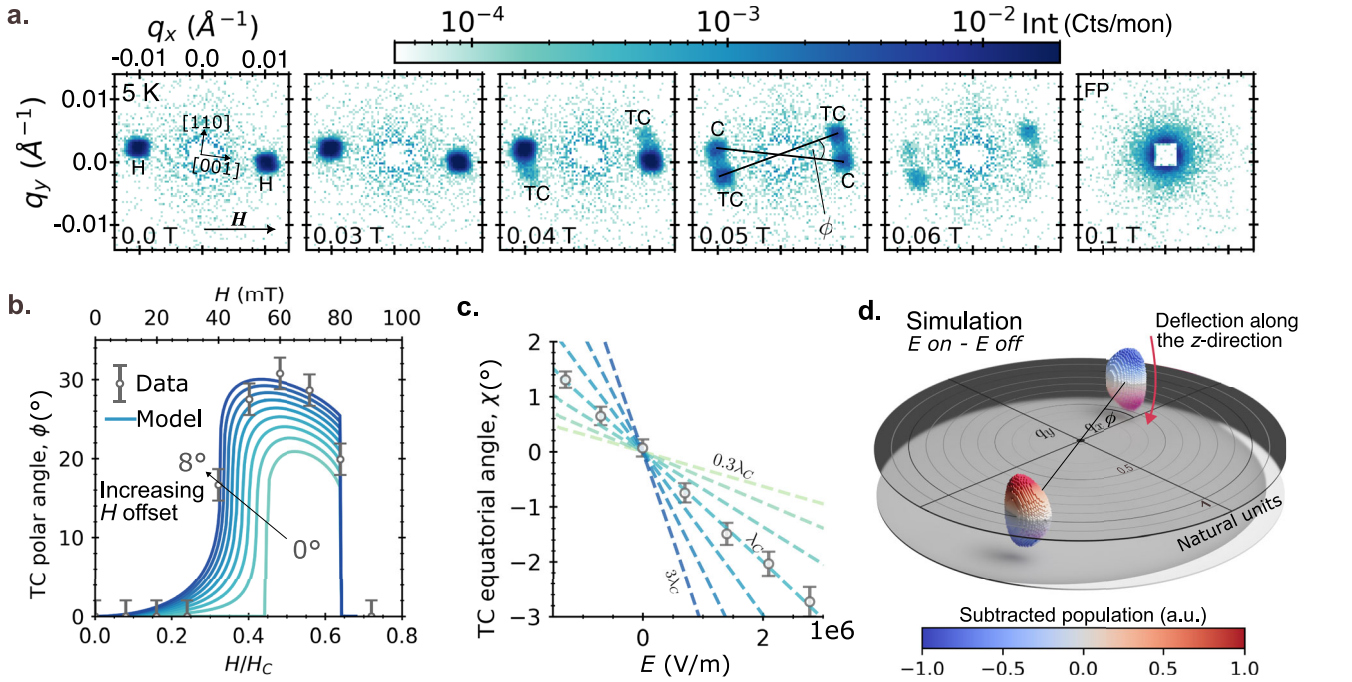

Fig. 4 | Continuum magnetic theory explaining the trajectory of the spiral deflection. a Series of rocked SANS patterns showing the evolution of the magnetic states from the helical ground state into a field-polarised state at 0.1 T, passing through an intermediate regime with coexisting tilted conical and conical states. **b** Theoretical calculations and experimental data for the TC polar angle as a function of the applied magnetic field. The TC deflection angle is simulated for a range of different fiel offsets from the [001]-direction. **c** Curves illustrating the dependence of the magnetoelectric response on the saturation polarisation, λ_C. A linear trend in the simulated TC trajectory is consistently observed around the refined value. **d** 3D reciprocal space difference map between the theoretical population of two states subjected to external fields of 0 and 2.5×10^6 V/m, respectively. Errors correspond to the diagonalised covariance matrix obtained in the fitting procedure.

response, therefore, primarily manifests directly from *EP*-coupling, dominating over secondary effects such as anisotropies arising from inverse piezoelectric deformations. With all constants established, we proceed to fully model the magnetoelectric deflection response of the TC texture by simulating the *E*-field dependent classical populations of the state, analogous to the intensity distributions measured with SANS. By subtracting two datasets simulated at different *E*-fields, we obtain a difference plot (Fig. 4d) showing fantastic agreement with the subtraction of the experimentally observed data shown in Fig. 2e.

Having confirmed our model successfully captures the physics underlying our experimental observations, we next theoretically investigate the effects of applying higher electric fields beyond those explored in our experiments, while remaining bounded below the breakdown voltage of the material[55]. In Fig. 5a, we simulate the expected magnetoelectric deflection response for a TC domain under two different applied magnetic fields and identify three distinct trajectory regimes. Moving past the linear *E*-field-dependence of χ found near $E = 0$ for $H = 0.5H_C$, an increase of the *E*-field first leads the system into a non-linear regime. Increasing the *E*-field further eventually leads to a flop of the magnetic wavevector, transitioning abruptly to a second type of TC domain oriented 90° from the original domain. In this configuration, the net polarisation of the second TC domain aligns fully with the *E*-field, no longer competing with the anisotropic magnetic interactions. For $H = 0.6H_C$, the trajectory of the deflection states similarly shifts from linear to non-linear behaviour as the *E*-field increases, with no wavevector flop observed within the bounds of the simulation.

The predicted emergence of these new trajectory regimes leads naturally to exciting expectations for novel ME coupling phenomena. In Fig. 5b, we demonstrate that one can continuously tune the onset *E*-field of these regimes and the gradient of their deflection trajectory by varying the applied magnetic field, uncovering an intricate interplay between competing ME coupling and anisotropic magnetic interactions. Figure 5c, d highlights further these response regimes. In the lower parts of each panel, we simulate the low-frequency deflection response for both the linear-regime (small *E*, large *H*) and flop-regime (large *E*, low *H*), respectively. In (c), we predict an in-phase and linear variation in χ for an oscillating electric field. Decreasing the applied magnetic field or increasing the magnitude of the *E*-field encourages the magnetoelectric response to enter into a non-linear regime, typically characterised by the appearance of extra odd-frequencies harmonics in the deflection response[35,56]. In contrast, the flop-regime exhibits bistable-like behaviour, with the entire state undergoing significant reorientation between two distinct TC domain states, aligning the electric polarisation of the newly populated domain to the applied *E*-field. This flop between the two states exhibits a small phase shift, influenced by the *H*-dependent anisotropy barrier required to flop the magnetic wavevector into the lower energy state. Although this study focuses on the zero-frequency limit, we anticipate a plethora of frequency-driven excitations as we approach the resonant modes of the deflection, typically occurring in the MHz to GHz regime for large-scale spin structures[57,58]. Finally, we emphasise the capability to customise the desired magnetoelectric deflection response in situ simply by adjusting the strength of the applied magnetic field. This distinctive behavior points to the potential for next-generational sensor technology, as deflections of the TC propagation direction generate macroscopic changes to both the net magnetisation and electric polarisation.

Our findings on the magnetoelectric behaviour of the TC texture differ significantly from previously reported *E*-field-induced skyrmion lattice rotations within the same material[29,59]. Specifically, the deflection direction of the TC state magnetic wavevector aligns with the *E*-field, while the skyrmion lattice in earlier studies remained fixed within the plane perpendicular to the magnetic field, regardless of the strength and direction of the *E*-field. Additionally, observing skyrmion

https://doi.org/10.1038/s41467-025-60288-1

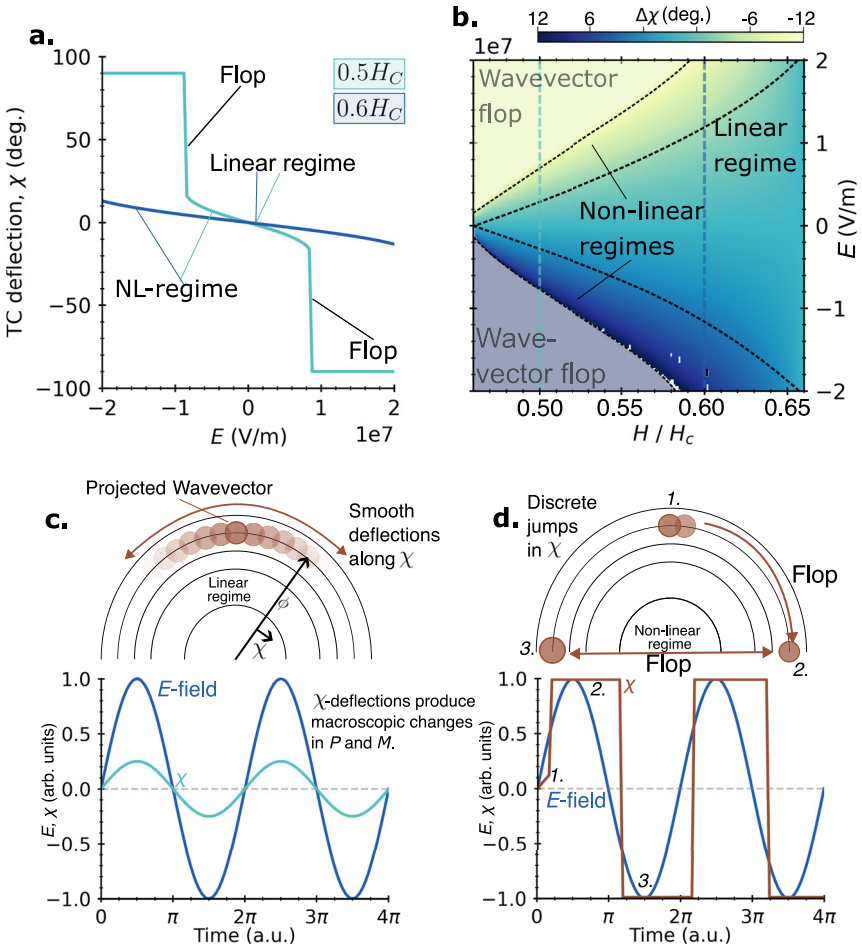

Fig. 5 | Functionality and variation of the magnetoelectric response. a Electric and magnetic field-induced variation of the TC state deflection, showing a transition from a linear regime at low *E*-fields into a non-linear regime for larger *E*-fields. Further increasing the magnitude of the applied *E*-field eventually induces a discontinuous flop of the TC propagation direction into that of a different TC domain state. The flop transition occurs at lower *E*-fields for a lower magnetic field. **b** Diagram depicting the nature of the magnetoelectric response as a function of the applied magnetic and electric field. Dashed lines indicate boundaries between the different regimes, drawn by eye after numerically differentiating the plot twice with respect to the applied *E*-field. **c**, **d** Schematic representations of the linear magnetic wavevector deflection and flop regimes. Semi-circles represent contours of constant ϕ, analogous to looking down the north-south pole in Fig. 2a. **c** The linear regime is characterised by a smooth and continuous deflection of the magnetic propagation direction along the χ direction, centered around $\chi = 0$. In a hypothetical alternating electric field scenario, the system response would be in-phase and proportional to the input *E*-field. **d** Ramping large *E*-fields rapidly causes the magnetic wavevector to flop, forming a distinct TC domain with a propagation direction located 90° away in χ. Subsequent cycles of opposite voltage skip over the intermediate $\chi = 0$, resulting in a bistable magnetoelectric response.

lattice rotations experimentally requires low-frequency excitations of the magnetic field[59]. In contrast, our observations of the TC state reveal distinct in situ deflection effects, which are anticipated to be further enriched by the onset of non-linear and flop-like deflection trajectories.

Despite considerable interest in magnetoelectric materials, the observation of such a macroscopic deflection, as reported here, has remained elusive. Previous investigations on one-dimensional incommensurate magnetic structures in other magnetoelectric materials have predominantly focused on systems hosting magnetic cycloid and transverse conical states exhibiting atomic-scale periodicities, such as the RMn_2O_3 series[4,60,61], as well as CuO and $LiCu_2O_2$[62–64]. In these materials, magnetoelectricity originates from the spin-current mechanism, generating electric polarisation between two spins ($\mathbf{S}_{i,j}$) separated by a position vector ($\mathbf{r}$) described by $\mathbf{P} \propto \mathbf{r} \times (\mathbf{S}_i \times \mathbf{S}_j)$. The net polarisation is inherently orthogonal to the magnetic propagation wavevector, meaning that any deflection to the propagation direction of these states does not reduce magnetoelectric energy under an applied *E*-field. Furthermore, significant magnetic anisotropy in these systems prevents a deflection of the magnetic wavevector, favoring instead a reversal of the symmetry-breaking spiral handedness in response to the applied *E*-field. To observe additional magnetoelectric deflection effects in materials, it is crucial to focus on those materials exhibiting the *d*-*p* hybridisation coupling mechanism, along with relatively weak magnetocrystalline anisotropies.

In our experiments, we primarily focused on the TC state; however, we intentionally cycled the magnetic field to create a coexistence state including the conical, TC and low-temperature skyrmion phases. This approach provides a comprehensive insight into the ME response of all the phases present. We observed that the low-temperature skyrmion and conical states do not exhibit any direct response to the *E*-field, as expected due to their negligible net electric polarisation. Nonetheless, it is intriguing to consider the potential effects of magnetoelectric deflection from a TC state at the interfaces between neighbouring domains of coexisting magnetic textures. The local magnetoelectric deflection in regions of the TC state in contact with isolated skyrmion states may provide a mechanism for tuning the local positions of the skyrmions. Alternatively, an intricate network of local TC domains could be deterministically nucleated using ion-beam methods[65], enabling dynamic control of magnetic skyrmions along

different paths using thermal gradients, similar to what has been observed with skyrmions and antiskyrmions moving down 1D helical 'racetracks'[66–68]. Direct visualisation mechanisms such as Lorentz transmission electron microscopy, scanning superconducting quantum interference devices or magnetic nanowire force microscopies could be employed to investigate these possibilities[69–71].

From our combined experimental and theoretical work, we have demonstrated a novel magnetoelectric response, in the form of a deflection of the propagation direction of an incommensurate magnetic state. The deflection mechanism we identify is rather general, indicating that magnetic materials that host both the d–p hybridisation ME coupling mechanism and competing anisotropies may show similar effects. This generality opens up the potential for room temperature applications in suitable materials and presents a significant opportunity to develop innovative functionalities in magnetoelectric devices.

Methods

Sample preparation

Single crystals of Cu_2OSeO_3 were grown from 5 g of thoroughly mixed stoichiometric amounts of CuO (99.99%, Alfa Aesar) and SeO_2 (99.999%, Thermo Scientific Chemicals) powders using the chemical vapour transport method. The powder, along with 2 mg/cc of TeCl4 transport agent, was sealed in a silica tube. The sealed tube was then placed in a two-zone furnace with the source maintained at 640 °C and the sink at 550 °C for 4 weeks. Several single crystals with dimensions of ~$4 \times 4 \times 4$ mm^3 were obtained. For the SANS experiment, one single crystal was shaped using a polishing wheel into a plate with dimensions $3.5 \times 4 \times 0.9$ mm^3 and a mass of 51.7 mg. The sample was polished such that there were two large, parallel $(1\bar{1}0)$ faces.

Magnetic property measurements

A quantum design magnetic property measurement system, MPMS3, superconducting quantum interference device magnetometer, was used to investigate the bulk magnetic properties of the sample as a function of both temperature and magnetic field. The single-crystal used for the SANS measurements was aligned such that $\mu_0 H \| [001]$ and magnetic field-dependent DC magnetic-susceptibility measurements were carried out between 5 K and 60 K in 2 K intervals by zero-field cooling to the temperature set-point and increasing the magnetic field from 0 to 100 mT in 1 mT steps. Numerical derivatives of the resulting magnetisation were calculated to obtain phase boundaries and ordering temperatures, with the first derivative plotted in Fig. 1b.

SANS measurement and tomographic maps

SANS measurements were performed at the SANS-I beamline at the Swiss Spallation Neutron Source SINQ, Paul Scherrer Institut, Switzerland, with incident neutrons of wavelength $\lambda_n = 8$ Å, at a wavelength resolution $\frac{\Delta\lambda}{\lambda} = 10\%$, and a collimator and detector distance of 18 m. The single crystal was mounted onto a dedicated E-field sample holder[72], with electrodes attached directly onto the large, flat (1 1 0) faces. The sample was placed within a horizontal-field cryomagnet and oriented such that $E \| n_0 \| [1\bar{1}0]$, and $H \perp n_0 \| [001]$, see configuration in Fig. 1c. In our experiment, we applied a slight magnetic field offset to intentionally break the TC domain degeneracy and promote the TC domain highlighted in red in Fig. 2a. The rocked SANS diffraction patterns were measured by rotating both the sample and cryomagnet together through an angular range of 14 degrees such that the diffraction spots completely passed through the diffraction condition. By calculating the momentum transfer required to diffract a neutron into each pixel of the detector, and by using information about the rocking angle, 3D tomographic SANS maps can be created as shown in Fig. 2. All measurements were taken at temperatures ranging from 5 K to 60 K and with magnetic fields ranging from 0–250 mT. Background measurements were carried out in the paramagnetic state at $T = 70$ K and in the field-polarised regime at 5 K, 250 mT. The cooling down procedure was from 60 to 5 K, before simultaneously ramping to the desired electric field and applying 40 magnetic field oscillations from 40 mT to 60 mT, see white arrows in Fig. 1. This procedure allowed a consistent coexisting state to be obtained at low temperatures.

Continuum-field model

Hamiltonian. Expanding upon the Bak-Jensen model to include the Zeeman and magnetoelectric terms, we model the complex network of effective interactions within Cu_2OSeO_3 using symmetry-consistent free energy density expansion valid for a slowly-varying magnetic field ($\mathbf{m}(\mathbf{r})$) such as the TC state. This is given by ref.[49]:

$$\begin{aligned} F(\mathbf{r}) = {} & D\mathbf{m}(\mathbf{r}) \cdot (\nabla \times \mathbf{m}(\mathbf{r})) \\ & + \frac{1}{2}A\left((\nabla m_x)^2 + (\nabla m_y)^2 + (\nabla m_z)^2\right) \\ & + \frac{1}{2}\gamma\left(\left(\frac{\partial m_x}{\partial x}\right)^2 + \left(\frac{\partial m_y}{\partial y}\right)^2 + \left(\frac{\partial m_z}{\partial z}\right)^2\right) \\ & + K\left(m_x^4 + m_y^4 + m_z^4\right) \\ & - \mu_0 M_s(\mathbf{m}(\mathbf{r}) \cdot \mathbf{H}) - \mathbf{P}(\mathbf{r}) \cdot \mathbf{E}, \end{aligned} \tag{3}$$

where D, A are the Dzyaloshinskii-Moriya and exchange stiffness constants, respectively. $\mathbf{H}$ and $\mathbf{E}$ denote the applied magnetic and electric fields. The anisotropy constants, K and γ, correspond to the 4th order magnetocrystalline anisotropy and anisotropic exchange interactions, respectively, and must assume specific values in order to stabilise a TC state[44,45]. Additional details about these terms can be found in the Supplementary Information.

Due to the one-dimensional and periodic nature of the magnetic textures studied here, we compute the average free energy density, $\bar{F}$, across a single conical period using:

$$\bar{F} = \frac{1}{\lambda}\int_0^{\lambda} F(\mathbf{r})\,\mathrm{d}\mathbf{r}, \tag{4}$$

where $\bar{F}$ represents the average free energy density along a path parallel to the propagation vector, $\mathbf{q}$. In micromagnetics, magnetic free energy densities are typically evaluated in three dimensions[73]. However, for the conical spin textures under consideration, the energy density varies only along the direction of $\mathbf{q}$, while remaining uniform in the other two orthogonal directions. By integrating along $\mathbf{q}$, we account for all relevant variations in the texture, and the contributions from the constant perpendicular directions can be excluded without loss of generality. This approach simplifies the calculation while remaining fully consistent with the dimensionality of the system.

In order to evaluate the stability and deflection of the TC state, we start with the continuum form of a general conical state with a wavevector pointing along an arbitrary direction:

$$\mathbf{m}(\mathbf{r})/M_s = \sin\theta\left(\cos(\mathbf{q}\cdot\mathbf{r})\hat{\mathbf{e}}_1 + \sin(\mathbf{q}\cdot\mathbf{r})\hat{\mathbf{e}}_2\right) + \cos\theta\hat{\mathbf{e}}_3, \tag{5}$$

where θ is the conical angle, and $\{\hat{\mathbf{e}}_n\}$ define three mutually orthogonal basis vectors, such that $\mathbf{q} \| \hat{\mathbf{e}}_3$. By using the same polar coordinate basis to define the wavevector, $\mathbf{q} = q(\sin\phi\cos\chi,\ \sin\phi\sin\chi,\ \cos\phi)$, together with an applied E-field along the $[1\bar{1}0]$ direction, inserting Eq. (5) into Eq. (3), integrating over one conical period to find the average free energy density before differentiating with respect to χ, we find:

$$\begin{aligned} \frac{\partial\bar{F}}{\partial\chi} = {} & \gamma\chi q^2\sin^2\theta\sin^4\phi \\ & + E\lambda_C\sin\phi\cos\phi(1+\chi)f(\theta) \\ & + K\chi\sin^4\phi g(\theta), \end{aligned} \tag{6}$$

Table 1 | Experimentally determined parameters used in the mean-field model

Constant	Value (SI)
Exch. stiffness, A	7×10^{-13} J/m[80]
DMI constant, D	7.4×10^{-5} J/m^2 [80]
Exch. anisotropy, γ	1×10^{-13} J/m[50]
Cubic anisotropy, K	320 J/m^3 [51]
Sat. Magnetisation, M_s	1.03 A/m[80]
Macroscopic Pol, λ_C	1.4×10^{-6} C/m^2 [81]
	10.2×10^{-6} C/m^2 [54]
	16×10^{-6} C/m^2 [53]
Our work	$10.4(4) \times 10^{-6}$ C/m^2

where the functions $f(\theta) = \frac{\sin^2\theta}{2} - \cos^2\theta$ and $g(\theta) = 24\sin^2\theta\cos^2\theta - 3\sin^4\theta - 4\cos^4\theta$ are dependent on the conical angle only. By inspection, we can see that in the absence of an external field E, a stable solution to the equation $\frac{\partial \bar{F}}{\partial \chi} = 0$ is found with $\chi = 0$. However, the $(1+\chi)$ term in Eq. (4) introduces a non-zero electric field to shift the solutions of the free energy density differential to finite values of χ. For small E, this yields the linear relationship presented in the main text. Detailed derivations of each term in Eq. (3) are available in ref. 74.

Experimental constants. The experimentally determined constants used in the mean-field model are shown below in Table 1.

Simulated populations of magnetic states. The populations of the magnetic states were generated using a classical theory, whereby the relative probability (P_i) of a state (i) being occupied compared to the lowest energy state follows a Boltzmann distribution[75]:

$$P_i \propto \exp^{-(E_i - E_0)/k_B T}, \tag{7}$$

where E_i is the energy of the state given by Eq. (3), with E_0 being the state of lowest energy. $k_B T$ is the temperature dependent Boltzmann function. In our population simulations, a temperature corresponding to $T \approx 5$ K was chosen to match the intensities found during the SANS experiment.

Visualisation methods

The three-dimensional reciprocal space maps were generated using custom Python code[76]. The output of the code was to export legacy `.vtk` files for generated a scenic `.x3d` file using Paraview[77,78]. These scenes were then rendered using Blender[79]. Inkscape was used throughout to create the composite figures.

Data availability

Experimental data and the relevant analysis scripts utilised to produce the presented figures are available from an online repository: https://gitea.psi.ch/moody_s/NCOMMS-25-19576-T/settings. Further material is available from the corresponding author upon reasonable request.

References

1. Greenwald, S. & Smart, J. S. Deformations in the crystal structures of anti-ferromagnetic compounds. *Nature* **166**, 523–524 (1950).
2. Schmid, H. Multi-ferroic magnetoelectrics. *Ferroelectrics* **162**, 317–338 (1994).
3. Fiebig, M., Lottermoser, T., Fröhlich, D., Goltsev, A. V. & Pisarev, R. V. Observation of coupled magnetic and electric domains. *Nature* **419**, 818–820 (2002).
4. Kimura, T. et al. Magnetic control of ferroelectric polarization. *Nature* **426**, 55–58 (2003).
5. Wang, J. et al. Epitaxial $BiFeO_3$ multiferroic thin film heterostructures. *Science* **299**, 1719–1722 (2003).
6. Eerenstein, W., Mathur, N. D. & Scott, J. F. Multiferroic and magnetoelectric materials. *Nature* **442**, 759–765 (2006).
7. Ramesh, R. & Spaldin, N. A. Multiferroics: progress and prospects in thin films. *Nat. Mater.* **6**, 21–29 (2007).
8. Cheong, S. W. & Mostovoy, M. Multiferroics: a magnetic twist for ferroelectricity. *Nat. Mater.* **6**, 13–20 (2007).
9. Fiebig, M., Lottermoser, T., Meier, D. & Trassin, M. The evolution of multiferroics. *Nat. Rev. Mater.* **1**, 1–14 (2016).
10. Spaldin, N. A. & Ramesh, R. Advances in magnetoelectric multiferroics. *Nat. Mater.* **18**, 203–212 (2019).
11. Fert, A., Ramesh, R., Garcia, V., Casanova, F. & Bibes, M. Electrical control of magnetism by electric field and current-induced torques. *Rev. Mod. Phys.* **96**, 015005 (2024).
12. Delaney, K. T., Mostovoy, M. & Spaldin, N. A. Superexchange-driven magnetoelectricity in magnetic vortices. *Phys. Rev. Lett.* **102**, 157203 (2009).
13. Picozzi, S., Yamauchi, K., Sanyal, B., Sergienko, I. A. & Dagotto, E. Dual nature of improper ferroelectricity in a magnetoelectric multiferroic. *Phys. Rev. Lett.* **99**, 227201 (2007).
14. Tokunaga, Y., Iguchi, S., Arima, T. & Tokura, Y. Magnetic-field-induced ferroelectric state in $DyFO_3$. *Phys. Rev. Lett.* **101**, 097205 (2008).
15. Katsura, H., Nagaosa, N. & Balatsky, A. V. Spin current and magnetoelectric effect in noncollinear magnets. *Phys. Rev. Lett.* **95**, 057205 (2005).
16. Mostovoy, M. Ferroelectricity in spiral magnets. *Phys. Rev. Lett.* **96**, 067601 (2006).
17. Seki, S., Ishiwata, S. & Tokura, Y. Magnetoelectric nature of skyrmions in a chiral magnetic insulator Cu_2OSeO_3. *Phys. Rev. B* **86**, 060403 (2012).
18. Yang, J. H. et al. Strong Dzyaloshinskii-Moriya interaction and origin of ferroelectricity in Cu_2OSeO_3. *Phys. Rev. Lett.* **109**, 107203 (2012).
19. Arima, T. Ferroelectricity induced by proper-screw type magnetic order. *J. Phys. Soc. Jpn.* **76**, 073702 (2007).
20. Gajek, M. et al. Tunnel junctions with multiferroic barriers. *Nat. Mater.* **6**, 296–302 (2007).
21. Evans, D. M. et al. Magnetic switching of ferroelectric domains at room temperature in multiferroic PZTFT. *Nat. Commun.* **4**, 1534 (2013).
22. Soda, M. et al. Continuous control of local magnetic moment by applied electric field in multiferroics $Ba_2CoGe_2O_7$. *Phys. Rev. B* **94**, 094418 (2016).
23. Walker, H. C. et al. Femtoscale magnetically induced lattice distortions in multiferroic $TbMnO_3$. *Science* **333**, 1273–1276 (2011).
24. Matsubara, M. et al. Magnetoelectric domain control in multiferroic $TbMnO_3$. *Science* **348**, 1112–1115 (2015).
25. Honda, T. et al. Coupled multiferroic domain switching in the canted conical spin spiral system Mn_2GeO_4. *Nat. Commun.* **8**, 15457 (2017).
26. Meier, D. & Selbach, S. M. Ferroelectric domain walls for nanotechnology. *Nat. Rev. Mater.* **7**, 157–173 (2022).
27. Okamura, Y., Kagawa, F., Seki, S. & Tokura, Y. Transition to and from the skyrmion lattice phase by electric fields in a magnetoelectric compound. *Nat. Commun.* **7**, 12669 (2016).
28. Kruchkov, A. J. et al. Direct electric field control of the skyrmion phase in a magnetoelectric insulator. *Sci. Rep.* **8**, 10466 (2018).
29. White, J. S. et al. Electric field control of the skyrmion lattice in Cu_2OSeO_3. *J. Phys. Condens. Matter* **24**, 432201 (2012).
30. Liang, X., Chen, H. & Sun, N. X. Magnetoelectric materials and devices. *APL Mater.* **9**, 041114 (2021).
31. Kopyl, S., Surmenev, R., Surmeneva, M., Fetisov, Y. & Kholkin, A. Magnetoelectric effect: principles and applications in biology and medicine– a review. *Mater. Today Bio* **12**, 100149 (2021).

32. Onsager, L. Crystal statistics. i. a two-dimensional model with an order-disorder transition. *Phys. Rev.* **65**, 117–149 (1944).
33. Neubauer, A. et al. Topological Hall effect in the *a* phase of MnSi. *Phys. Rev. Lett.* **102**, 186602 (2009).
34. Schulz, T. et al. Emergent electrodynamics of skyrmions in a chiral magnet. *Nat. Phys.* **8**, 301–304 (2012).
35. Furuta, S., Moody, S. H., Kado, K., Koshibae, W. & Kagawa, F. Energetic perspective on emergent inductance exhibited by magnetic textures in the pinned regime. *npj Spintronics* **1**, 1 (2023).
36. *Principles of Neutron Scattering from Condensed Matter* (Oxford University Press, 2020) https://books.google.ch/books?id=fSvsDwAAQBAJ.
37. Blundell, S. *Magnetism in Condensed Matter*. In: Oxford Master Series in Condensed Matter Physics (OUP Oxford, 2001). https://books.google.ch/books?id=zP9QEAAAQBAJ.
38. Nagaosa, N. & Tokura, Y. Topological properties and dynamics of magnetic skyrmions. *Nat. Nanotechnol.* **8**, 899–911 (2013).
39. Kohn, K. A new ferrimagnet Cu_2SeO_4. *J. Phys. Soc. Jpn.* **42**, 2065–2066 (1977).
40. Bos, J. W. G., Colin, C. V. & Palstra, T. T. M. Magnetoelectric coupling in the cubic ferrimagnet Cu_2OSeO_3. *Phys. Rev. B* **78**, 094416 (2008).
41. Mühlbauer, S. et al. Skyrmion lattice in a chiral magnet. *Science* **323**, 915–919 (2009).
42. Janson, O. et al. The quantum nature of skyrmions and half-skyrmions in Cu_2OSeO_3. *Nat. Commun.* **5**, 5376 (2014).
43. Littlehales, M. T. et al. Demonstration of controlled skyrmion injection across a thickness step. *Nano Lett.* **24**, 6813–6820 (2024).
44. Moody, S. H. et al. Experimental evidence of a change of exchange anisotropy sign with temperature in Zn-substituted Cu_2OSeO_3. *Phys. Rev. Res.* **3**, 043149 (2021).
45. Qian, F. et al. New magnetic phase of the chiral skyrmion material Cu_2OSeO_3. *Sci. Adv.* **4**, eaat7323 (2018).
46. Chacon, A. et al. Observation of two independent skyrmion phases in a chiral magnetic material. *Nat. Phys.* **14**, 936–941 (2018).
47. Crisanti, M. et al. Tilted spirals and low-temperature skyrmions in Cu_2OSeO_3. *Phys. Rev. Res.* **5**, 033033 (2023).
48. Mühlbauer, S. et al. Magnetic small-angle neutron scattering. *Rev. Mod. Phys.* **91**, 015004 (2019).
49. Bak, P. & Jensen, M. H. Theory of helical magnetic structures and phase transitions in MnSi and FeGe. *J. Phys. C: Solid State Phys.* **13**, L881 (1980).
50. Baral, P. R. et al. Direct observation of exchange anisotropy in the helimagnetic insulator Cu_2OSeO_3. *Phys. Rev. Res.* **5**, L032019 (2023).
51. Halder, M. et al. Thermodynamic evidence of a second skyrmion lattice phase and tilted conical phase in Cu_2OSeO_3. *Phys. Rev. B* **98**, 144429 (2018).
52. Mochizuki, M. Microwave magnetochiral effect in Cu_2OSeO_3. *Phys. Rev. Lett.* **114**, 197203 (2015).
53. Mochizuki, M. & Seki, S. Magnetoelectric resonances and predicted microwave diode effect of the skyrmion crystal in a multiferroic chiral-lattice magnet. *Phys. Rev. B* **87**, 134403 (2013).
54. Omrani, A. A. et al. Exploration of the helimagnetic and skyrmion lattice phase diagram in Cu_2OSeO_3 using magnetoelectric susceptibility. *Phys. Rev. B* **89**, 064406 (2014).
55. Han, M.-G. et al. Hysteretic responses of skyrmion lattices to electric fields in magnetoelectric Cu_2OSeO_3. *Nano Lett.* **23**, 7143–7149 (2023).
56. Nakano, H. Linear response theory: a historical perspective. *Int. J. Mod. Phys. B* **07**, 2397–2467 (1993).
57. Lancaster, T. et al. Transverse field muon-spin rotation signature of the skyrmion-lattice phase in Cu_2OSeO_3. *Phys. Rev. B* **91**, 224408 (2015).
58. Hicken, T. J. et al. Megahertz dynamics in skyrmion systems probed with muon-spin relaxation. *Phys. Rev. B* **103**, 024428 (2021).
59. White, J. S. et al. Electric-field-induced skyrmion distortion and giant lattice rotation in the magnetoelectric insulator Cu_2OSeO_3. *Phys. Rev. Lett.* **113**, 107203 (2014).
60. Kenzelmann, M. et al. Magnetic inversion symmetry breaking and ferroelectricity in $TbMnO_3$. *Phys. Rev. Lett.* **95**, 087206 (2005).
61. Vajk, O. P., Kenzelmann, M., Lynn, J. W., Kim, S. B. & Cheong, S.-W. Magnetic order and spin dynamics in ferroelectric Ho_2PdSi_3. *Phys. Rev. Lett.* **94**, 087601 (2005).
62. Kimura, T., Sekio, Y., Nakamura, H., Siegrist, T. & Ramirez, A. P. Cupric oxide as an induced-multiferroic with high-TC. *Nat. Mater.* **7**, 291–294 (2008).
63. Seki, S. et al. Correlation between spin helicity and an electric polarization vector in quantum-spin chain magnet $LiCu_2O_2$. *Phys. Rev. Lett.* **100**, 127201 (2008).
64. Lebeugle, D. et al. Electric-field-induced spin flop in $LiCu_2O_2$ single crystals at room temperature. *Phys. Rev. Lett.* **100**, 227602 (2008).
65. Kern, L. M. et al. Deterministic generation and guided motion of magnetic skyrmions by focused He^+-ion irradiation. *Nano Lett.* **22**, 4028–4035 (2022).
66. Müller, J. et al. Magnetic skyrmions and skyrmion clusters in the helical phase of Cu_2OSeO_3. *Phys. Rev. Lett.* **119**, 137201 (2017).
67. Knapman, R., Rodrigues, D. R., Masell, J. & Everschor-Sitte, K. Current-induced h-shaped-skyrmion creation and their dynamics in the helical phase. *J. Phys. D: Appl. Phys.* **54**, 404003 (2021).
68. He, Z. et al. Experimental observation of current-driven anti-skyrmion sliding in stripe domains. *Nat. Mater.* **23**, 1048–1054 (2024).
69. Yu, X. Z. et al. Real-space observation of a two-dimensional skyrmion crystal. *Nature* **465**, 901–904 (2010).
70. Marchiori, E. et al. Nanoscale magnetic field imaging for 2D materials. *Nat. Rev. Phys.* **4**, 49–60 (2022).
71. Rossi, N. et al. Vectorial scanning force microscopy using a nanowire sensor. *Nat. Nanotechnol.* **12**, 150–155 (2017).
72. Bartkowiak, M., White, J. S., Rønnow, H. M. & Prša, K. Note: Versatile sample stick for neutron scattering experiments in high electric fields. *Rev. Sci. Instrum.* **85**, 026112 (2014).
73. Landau, L. & Lifshitz, E. On the theory of the dispersion of magnetic permeability in ferromagnetic bodies. *Phys. Z. Sov. Union* **8**, 101–114 (1935).
74. Moody, S. H. *Probing the Nature of the Magnetic Interactions in Magnetic Skyrmions*. PhD thesis, Durham University. Available at https://etheses.dur.ac.uk/14945/ (2023).
75. Maxwell, J. C. IV. On the dynamical theory of gases. In *Philosophical transactions of the Royal Society of London* 49–88 (1867).
76. Van Rossum, G. & Drake Jr, F. L. *Python reference manual* (Centrum voor Wiskunde en Informatica Amsterdam, 1995).
77. Ahrens, J. P., Geveci, B. & Law, C. C. Paraview: an end-user tool for large-data visualization. In *The Visualization Handbook* (2005).
78. Ayachit, U. *The ParaView guide: a parallel visualization application* (Kitware, Inc., Clifton Park, NY, USA, 2015).
79. Community, B. O. *Blender - a 3D modelling and rendering package*. Blender Foundation, Stichting Blender Foundation, Amsterdam http://www.blender.org (2018).
80. Zhang, S. et al. Reciprocal space tomography of 3d skyrmion lattice order in a chiral magnet. *Proc. Natl Acad. Sci.* **115**, 6386–6391 (2018).
81. Ruff, E., Lunkenheimer, P., Loidl, A., Berger, H. & Krohns, S. Magnetoelectric effects in the skyrmion host material cu2oseo3. *Sci. Rep.* **5**, 15025 (2015).

Acknowledgements

This work was supported by the UK Skyrmion Project EPSRC Programme Grant (No. EP/N032128/1, P.D.H/G.B.), and the Swiss National Science Foundation project (No. 200021_188707, J.S.W.). The work at the University of Warwick was also supported by EPSRC through Grant EP/T005963/1 (G.B./D.M.). The SANS experiments were performed at the

Swiss spallation neutron source SINQ, Paul Scherrer Institute, Villigen, Switzerland, under Proposal No. 20221453. M.T.L. acknowledges the financial support of the Science and Technology Facilities Council (STFC) and the ISIS Neutron and Muon Source in the form of an ISIS facility development studentship. We are grateful for the assistance of M. Bartkowiak for aiding with the setup of the electric field experiments. We gratefully acknowledge the provision of the MPMS3 in the ISIS Neutron and Muon Source Materials Characterisation Laboratory.

Author contributions

S.H.M. and P.D.H. conceived the project. S.H.M. and M.T.L. performed the magnetization measurements. S.H.M., M.T.L., D.A.V. and J.S.W. performed the SANS measurements. G.B. and D.M. provided the samples used in this study. S.H.M. performed the analysis and developed the theoretical model. All authors contributed to the editing and writing of the manuscript.

Competing interests

The authors declare no competing interests.

Additional information

Supplementary information The online version contains supplementary material available at https://doi.org/10.1038/s41467-025-60288-1.

Correspondence and requests for materials should be addressed to Samuel H. Moody or Jonathan S. White.

Peer review information *Nature Communications* thanks the anonymous, reviewers for their contribution to the peer review of this work. A peer review file is available.